第 31 卷第 5 期
2025 年 10 月

地 质 力 学 学 报
JOURNAL OF GEOMECHANICS

Vol. 31 No. 5
Oct. 2025

引用格式：王允腾，王亚东，刘嘉欣，等，2025. 岩土体非连续结构演化的相场模拟方法[J]. 地质力学学报，31（5）：869−885. DOI：10.12090/j.issn.1006-6616.2025149

Citation: WANG Y T，WANG Y D，LIU J X，et al.，2025. Phase–field modelling of discontinuous structures in geomaterials[J]. Journal of Geomechanics，31（5）：869−885. DOI：10.12090/j.issn.1006-6616.2025149

岩土体非连续结构演化的相场模拟方法

王允腾，王亚东，刘嘉欣，康　璇，吴　伟
WANG Yunteng，WANG Yadong，LIU Jiaxin，KANG Xuan，WU Wei

维也纳自然资源与生命科学大学岩土工程研究所，奥地利 维也纳 1180
Institute of Geotechnical Engineering, *BOKU University*, *Vienna* 1180, *Austria*

Phase–field modelling of discontinuous structures in geomaterials

Abstract: ［**Objective**］This study aims to develop a thermodynamically consistent phase–field framework for modeling the initiation and evolution of discontinuous structures in geomaterials.［**Methods**］Our model introduces crack driving forces derived from the volumetric–deviatoric strain decomposition strategy, incorporating distinct tension, compression, and shear degradation mechanisms. Inertia effects capture compaction-band formation driven by wave-like disturbances, grain crushing, and frictional rearrangement. A monolithic algorithm ensures numerical stability and rapid convergence.［**Results**］The framework reproduces tensile, shear, mixed tensile–shear, and compressive–shear failures using the Benzeggagh–Kenane criterion. Validation against benchmark simulations—including uniaxial compression of rock-like and triaxial compression of V-notched sandstone specimens—demonstrates accurate predictions of crack initiation stress, localization orientation, and energy dissipation.［**Conclusions**］The framework provides a unified and robust numerical tool for analyzing the spatiotemporal evolution of strain localization and fracture in geomaterials.［**Significance**］By linking microscale fracture dynamics with macroscale failure within a thermodynamically consistent scheme, this study advances predictive modeling of rock stability, slope failure, and subsurface energy systems, contributing to safer and more sustainable geotechnical practice.

Keywords: rock cracks; localized deformation bands; multiscale characteristics; phase–field model; numerical simulations

摘　要：文章建立了一种热力学一致的相场框架，用于描述地质材料在复杂应力条件下不连续结构的起裂与演化。模型基于体积−偏应变分解的裂纹驱动力，区分拉伸、压缩与剪切退化机制，并引入惯性效应以反映压实带形成中的波动扰动、颗粒破碎与摩擦重排。采用整体耦合算法，提高了计算的稳定性与收敛性。结果表明，该框架可依托 Benzeggagh–Kenane 准则准确再现拉伸、剪切及复合破坏模式，并在单轴压缩与 V 形缺口砂岩三轴压缩算例中成功预测裂纹起裂应力、局部化取向及能量耗散，与实验结果吻合良好。该框架可统一刻画地质材料在拉伸、压缩与剪切耦合作用下的局部化与破裂演化，为复杂加载条件下岩体破坏机理研究提供了稳健的理论与数值工具。

关键词：岩石裂纹；局部化变形带；多尺度特征；相场法；数值模拟

中图分类号：X43; TU9　　**文献标识码：**A　　**文章编号：**1006−6616(2025)05−0869−17

基金项目：欧盟委员会“地平线欧洲”框架计划玛丽·居里学者行动——人才交流项目（101129729，101182721，101235182）；欧洲研究委员会高级研究员资助项目（101141312）；奥地利国家科学基金项目（M3340，P37175）

This research is financially supported by the Horizon Europe Marie Skłodowska-Curie Actions Staff Exchanges Projects of the European Commission: LOC3G (Grant No. 101129729), MONUGEO (Grant No. 101182721), and SAFARI (Grant No. 101235182), the Advanced Grant MOTRAN of the European Research Council (ERC) (Grant No. 101141312), and the Austrian Science Fund (FWF) Projects: MultiCBPR (Grant No. M3340) and HIME (Grant No. P37175).

第一作者：王允腾（1990—），男，博士，特聘教授，主要从事计算岩土力学研究。Email: yunteng.wang@boku.ac.at

通信作者：吴伟（1961—），男，博士，讲席教授，主要从事岩土力学与岩土工程研究。Email: wei.wu@boku.ac.at

收稿日期：2025−10−09；**修回日期：**2025−10−17；**录用日期：**2025−10−22；**网络出版日期：**2025−10−22；**责任编辑：**王婧

DOI：10.12090/j.issn.1006-6616.2025149

0 Introduction

Discontinuous structures are inherent features of geomaterials such as soils and rocks, and they play a decisive role in controlling deformation, strength, and fluid transport properties (Darve et al., 2004; Selvadurai and Yu, 2005; Gudehus and Karcher, 2024). Broadly, these discontinuities can be categorized into two fundamental types: fractures (Hoek, 1968) and deformation bands (Rudnicki and Rice, 1975), as shown in Suppl. Fig. 1. A fracture corresponds to the initiation and propagation of cracks that create new free surfaces within otherwise intact material. From a mathematical perspective, fractures represent a "strong discontinuity", characterized by displacement jumps across the fracture plane. In contrast, a deformation band is a narrow zone of localized inelastic strain where grains undergo rearrangement, crushing, or sliding without the creation of entirely new surfaces. This behavior is typically described as a "weak discontinuity" (Rudnicki and Rice, 1975; Vardoulakis, 1980), in which strain, rather than displacement, is discontinuous across the band.

Both fractures and deformation bands exhibit systematic variations depending on the prevailing stress conditions. Fractures are commonly classified into three fundamental modes (Hoek, 1968; Ingraffea and Heuze, 1980): tensile fractures (Mode I), which open perpendicular to the least compressive stress; in-plane shear fractures (Mode II), which result from sliding along the fracture surface parallel to the maximum shear stress; and out-of-plane shear fractures (Mode III), involving tearing motions orthogonal to the fracture front. Similarly, deformation bands can be grouped into three principal types: dilation bands, where localized grain separation increases porosity; shear bands, characterized by intense grain sliding and shear offset; and compaction bands, where localized pore collapse leads to densification and permeability reduction (Fossen and Bale, 2007; Fossen et al., 2011).

The presence of discontinuous structures exerts a decisive influence on the mechanical response of geomaterials and thus plays a pivotal role in the stability and safety of geotechnical systems. These discontinuities not only govern deformation and strength characteristics but also control fluid transport, energy dissipation, and failure evolution across a wide range of engineering applications. Owing to their inherent multiscale features, from grain-scale defects to large-scale faults (as seen in Suppl. Fig. 2), and their interactions with multiphysical environments such as thermo–hydro–mechanical–chemical (THMC) couplings, the failure behavior of discontinuities is highly complex and remains a central challenge in geomechanics. It can be observed from Suppl. Fig. 2 that formations of rock fracture process zones and compaction bands are closely related to the microstructural evolution, which can be observed in laboratory (Fossen et al., 2011; Cheng and Wong, 2018; Zhang and Zhou, 2022).

Therefore, a better understanding of these behaviors is essential for advancing predictive models and developing numerical tools for geotechnical engineering. Some representative examples highlight the critical relevance of discontinuities to geo-engineering practice: (i) rock spalling and slabbing during tunnel excavation (see Suppl. Fig. 3a), initiation and evolution of sliding surfaces in rockslides and landslides in the extreme climate changing environment (see Suppl. Fig. 3b), fault rupture propagation during seismic events (see Suppl. Fig. 3c), and fracture network development in hydraulic stimulation for geothermal and energy storage projects (see Suppl. Fig. 3d). Each of these processes is inherently controlled by the nucleation, interaction, and evolution of discontinuous structures under complex stress and environmental conditions. Consequently, unraveling the mechanisms that govern the initiation, propagation, and coalescence of fractures and deformation bands represents one of the foremost scientific and engineering challenges in modern geotechnical research. Tackling these challenges is fundamental for improving hazard assessment, enhancing the resilience of infrastructures, and enabling the safe and sustainable exploitation of subsurface resources.

Over the past several decades, systematic laboratory investigations have significantly advanced our understanding of fracture behavior in rocks subjected to diverse loading paths（Vajdova and Wong, 2003; Baud et al., 2004, 2017; Huang et al., 2019; Abdallah et al., 2021; Leuthold et al., 2021; Zhang and Zhou, 2022）. These studies have identified key micromechanical processes, including microcrack nucleation, wing-crack growth, shear-band localization, pore collapse, and ultimate macroscopic faulting, that govern brittle and quasi-brittle failure. The advanced imaging and monitoring techniques such as acoustic emission, X-ray microtomography, neutron diffraction, and digital image correlation have further revealed the spatiotemporal evolution of discontinuities (Zhang and Zhou, 2022). Yet, despite these breakthroughs, laboratory observations are inherently limited by specimen size effects, boundary conditions, testing costs, and the resolution of diagnostic tools, making it challenging to extrapolate experimental results directly to field-scale rock masses where multiscale interactions and geological heterogeneities dominate.

In parallel, numerical modeling has become indispensable for complementing experiments and bridging the gap to engineering scales. A wide spectrum of computational strategies has been proposed for simulating discontinuous deformation, including the discrete element method for grain-scale processes (Potyondy and Cundall, 2004; Bertrand et al., 2008; Wautier et al., 2019; Wang et al., 2024a), the extended finite element method for explicit crack representation (Moës et al., 1999; Moës and Belytschko, 2002; Cruz et al., 2018; Hong et al., 2024), peridynamics for long-range interactions (Silling, 2000; Silling and Askari, 2005; Silling et al., 2007; Wang et al., 2016; Zhou and Wang, 2021; Wang and Wu, 2023), and more recently, the phase–field method (Francfort and Marigo, 1998; Bourdin et al., 2000; Miehe et al., 2010; Wu, 2017; Liu et al., 2022; Wang et al., 2023; Liu and Wang, 2025), which offers an elegant variational framework. The latter has been particularly influential, as it naturally captures fracture initiation, propagation, branching, and coalescence without requiring explicit crack tracking or remeshing. By introducing an intrinsic length scale parameter, the phase–field approach regularizes sharp cracks into diffuse interfaces, while the energy minimization principle provides a unified means of coupling displacement fields with fracture evolution (Ip and Borja, 2022, 2023). Moreover, the phase–field approach is well suited for simulating the evolution of discontinuous structures due to the inclusion of a characteristic length in the governing equations. As shown in Suppl. Fig. 4a, discontinuous structures in the phase–field formulation can be represented as diffuse damage zones consisting of a primary fault and surrounding microcracks. This diffuse damage morphology is consistent with experimental observations of fracture process zones in rocks (Suppl. Fig. 4b) and shear bands in soils (Suppl. Fig. 4c). Both laboratory experiments and in-situ field observations indicate that fracture process zones and shear bands exhibit a finite thickness, which is a manifestation of nonlocal behavior (Desrues and Chambon, 2002; Zhang and Zhou, 2022; Wang et al., 2024b). Such discontinuous yet nonlocal phenomena can be reproduced by modern numerical methods through nonlocal parameters, specifically the characteristic length in the phase–field approach.

Despite this progress, the simulation of compressive failure in rocks remains a formidable challenge. Unlike purely tensile cracking, compression-dominated regimes involve the coexistence and competition of tensile wing cracks, shear faulting, compaction bands, and mixed-mode fracture, which evolve dynamically under complex stress conditions. The standard phase–field formulations—often based on spectral decomposition or volumetric–deviatoric strain splitting—can reproduce tensile-driven fracture (Amor et al., 2009; Lee et al., 2016; Wu, 2017) but typically fail to capture shear-dominated rupture and compression-induced damage. To address this, several model extensions have emerged (Zhang et al., 2017; Wang et al., 2020; Fei and Choo, 2021; Liu et al., 2022; Hug et al., 2022). The stress-decomposition schemes allow different critical energy release rates for tensile and shear cracking, while others embed rock mechanics parameters such as cohesion, dilation, and friction angle into the crack-driving force, thereby aligning phase–field models more closely with classical strength theories. Such approaches have successfully simulated processes like double-crack coalescence and hydraulic stimulation in heterogeneous reservoirs（Heider, 2021）.

Recent developments have pushed this frontier further. Dual phase–field formulations, in which independent scalar fields represent tensile and shear cracking (Fei and Choo, 2021; Cao et al., 2022), provide a more nuanced description of mixed-mode fracture. Nonetheless, many of these models oversimplify by treating fracture as a binary tensile–shear process, limiting their ability to predict complex fracture networks where tensile, shear, and compactive features interact. More advanced formulations have begun to integrate Mohr–Coulomb, Hoek–Brown, and unified tensile–shear criteria within the variational phase–field framework, representing a promising synthesis between traditional rock mechanics theories and modern computational fracture mechanics.

Despite these advances, several critical research gaps remain. First, existing formulations often treat tensile–shear degradation and compressive–shear degradation separately, with few models capable of capturing their simultaneous and competitive evolution. Yet in real geological settings, such as landslide initiation, fault rupture, and reservoir stimulation—rocks experience highly heterogeneous stress fields where these mechanisms interact across scales. Second, most phase–field models have been developed in the context of mechanical fracture alone, with limited integration of multiphysical couplings involving fluid flow, heat transfer, chemical reactions, and grain-scale breakage. These couplings are increasingly recognized as critical in processes such as hydraulic fracturing, CO_2 injection, geothermal stimulation, and earthquake rupture. Third, there remains a need for rigorous experimental calibration and validation across scales, as the intrinsic length parameters and degradation functions used in phase–field models are often treated phenomenologically.

Looking ahead, the field is moving toward the development of unified, multiscale, and multiphysical fracture frameworks that integrate micromechanics-based homogenization, nonlocal continuum theories, and digital twin environments with advanced phase–field formulations. Such approaches have the potential to capture the full hierarchical nature of rock fracture, from grain rearrangement and pore collapse to fault-scale rupture. The convergence of high-resolution experiments, data-driven upscaling, and robust computational methods thus represents a frontier challenge in modern geomechanics, with far-reaching implications for the stability of geotechnical structures, the mitigation of natural hazards in environmental geotechnics, and the sustainable exploitation of subsurface resources in energy geotechnics.

1 Phase–field methodology for brittle fracture

Let us consider arbitrary solid computational domain Ω bounded by $\partial\Omega$ consisting of the sharp discontinuity Γ, as shown in Fig. 1. The boundary can be classified into the Dirichlet boundary $\partial\Omega_u$ and the Neumann boundary $\partial\Omega_t$ with $\partial\Omega = \partial\Omega_u \bigcup \partial\Omega_t$ and $\partial\Omega_u \bigcap \partial\Omega_t = \varnothing$. In the phase–field framework, sharp discontinuity can be regularized into the more diffuse damage zone Γ_{ℓ_c} by the phase–field variable d and the characteristic length of a material ℓ_c. Using the following crack surface density function $\gamma(d, \nabla d)$, we can describe the diffuse crack topology as follows,

$$\gamma(d, \nabla d) = \frac{1}{2\ell_c} d^2 + \frac{\ell_c}{2} |\nabla d|^2 \tag{1}$$

$$\Gamma_{\ell_c} \approx \int_{\Omega} \gamma(d, \nabla d)\, d\Omega \tag{2}$$

where d is the phase–field variable ranging from zero to one; and ℓ_c represents the characteristic length that is a nonlocal parameter for a material. The characteristic length ℓ_c also enables to measure the thickness of a fracture process zone or a deformation band. When $d = 0$, it indicates that the solid material is contact. While $d = 1$ means that the solid material is fully failed, as shown in Fig. 1.

The total potential energy of the continuum solid body Ω with the discontinuous structure Γ is composed of the stored elastic energy in solid and the surface energy stemming from the initiation and propagation of the discontinuous structure. The corresponding total potential energy function $\Psi(\boldsymbol{\varepsilon})$ is formulated as

$$\Psi(\boldsymbol{\varepsilon}) = \int_{\Omega \backslash \Gamma} \psi_0(\boldsymbol{\varepsilon})\, d\Omega + \int_{\Gamma} \mathcal{G}_c\, d\Gamma \tag{3}$$

in which $\psi_0(\boldsymbol{\varepsilon})$ is the stored elastic energy density, and $\mathcal{G}_c$ represents the critical energy release rate in Linear Elastic Fracture Mechanics. The initial stored elastic energy density $\psi_0(\boldsymbol{\varepsilon})$ can be written as

$$\psi_0(\boldsymbol{\varepsilon}) = \frac{\lambda}{2} \mathrm{Tr}(\boldsymbol{\varepsilon})^2 + \mu \boldsymbol{\varepsilon} : \boldsymbol{\varepsilon} \tag{4}$$

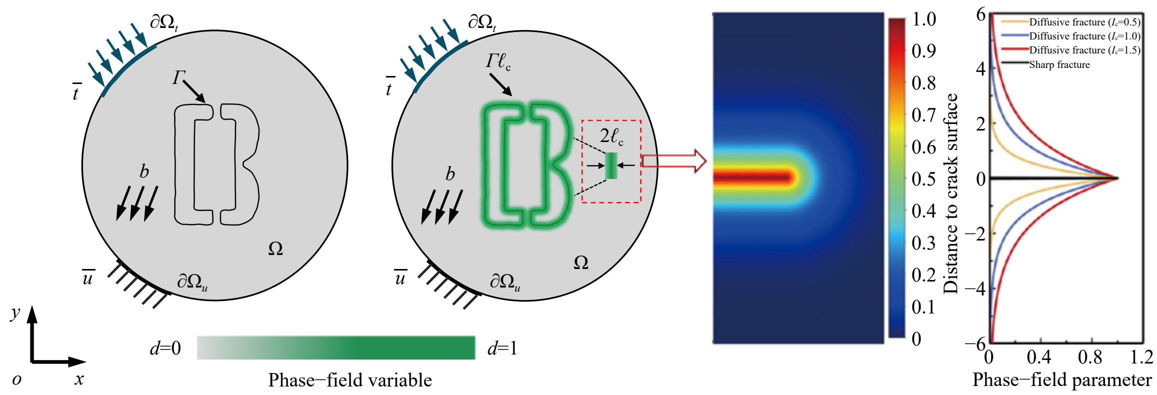

图 1　具有特征长度ℓ_c的弥散损伤区Γ_{ℓ_c}在相场法示意图

Fig. 1　Schematic diagram of phase–field method for a diffuse damage zone with a characteristic length

where λ and μ are Lamé constants, and $\boldsymbol{\varepsilon}=\frac{1}{2}\left(\nabla \boldsymbol{u}+(\nabla \boldsymbol{u})^{T}\right)$ is the strain tensor, where $\boldsymbol{u}$ denotes the displacement field.

To describe the total potential energy during the evolution of the discontinuous structure Γ_{ℓ_c} in the solid Ω, the functional total potential energy reads

$$\Psi_{\ell_c}(\boldsymbol{\varepsilon},d)=\underbrace{\int_{\Omega} g(d)\psi_0(\boldsymbol{\varepsilon})\,d\Omega}_{\Psi_0(\boldsymbol{\varepsilon},d)}+\underbrace{\int_{\Omega}\mathcal{G}_c\gamma(d,\nabla d)\,d\Omega}_{\Psi_f(d)} \tag{5}$$

where $g(d)$ is the degradation function to describe the remaining elastic strain energy stored in the solid (Miehe et al., 2010; Kuhn et al., 2015) which is expressed as

$$g(d)=\left[(1-d)^2+k\right] \tag{6}$$

where k is a positive constant for avoiding numerical instability (Miehe et al., 2010).

According to the variational principle for brittle fracture (Francfort and Marigo, 1998; Miehe et al., 2010), the Euler-Lagrange free energy functional $\Pi(\boldsymbol{\varepsilon},\Gamma)$ can be approximated as the following form in the phase–field model.

$$\begin{aligned}\Pi(\boldsymbol{\varepsilon},\Gamma)\simeq\Pi_{\ell_c}(\boldsymbol{\varepsilon},d)&=\Psi_{\ell_c}(\boldsymbol{\varepsilon},d)-W_{\text{ext}}(\boldsymbol{b},\boldsymbol{t},\boldsymbol{u})\\&=\int_{\Omega}\psi_{\ell_c}(\boldsymbol{\varepsilon},d)\,d\Omega+\int_{\Omega}\mathcal{G}_c\gamma(d,\nabla d)\,d\Omega-\\&\quad\int_{\Omega}\boldsymbol{b}^T\cdot\boldsymbol{u}\,d\Omega-\int_{\partial\Omega_t}\bar{\boldsymbol{t}}^T\cdot\boldsymbol{u}\,dS\end{aligned} \tag{7}$$

where $\boldsymbol{b}$ is the body force vector and $\bar{\boldsymbol{t}}$ denotes the prescribed traction vector.

In the original phase–field model (Miehe et al., 2010), the total strain energy decomposed the elastic strain energy into tensile and compressive parts to capture tensile brittle fractures.

$$\psi_{\ell_c}(\boldsymbol{\varepsilon},d)=\left[(1-d)^2+k\right]\psi_0^+(\boldsymbol{\varepsilon})+\psi_0^-(\boldsymbol{\varepsilon}) \tag{8}$$

where $\psi_0^{\pm}(\boldsymbol{\varepsilon})$ are the tensile and compressive parts of stored energy density.

In this work, we decompose the strain tensor into the volumetric part and deviatoric part as follows,

$$\boldsymbol{\varepsilon}=\boldsymbol{\varepsilon}_{\text{sph}}+\boldsymbol{\varepsilon}_{\text{dev}} \tag{9}$$

in which $\boldsymbol{\varepsilon}_{\text{sph}}$ represents the volumetric part of a strain tensor; and $\boldsymbol{\varepsilon}_{\text{dev}}$ is the deviatoric strain tensor.

In this work, we decompose the stored energy density function ψ_{ℓ_c} consisting of three parts: the pure dilational part ψ_n^+, the pure compressive part ψ_n^- and the tensile/compressive–shear part ψ_t.

$$\psi_{\ell_c}(\boldsymbol{\varepsilon},d)=\psi_n^+(\boldsymbol{\varepsilon},d)+\psi_t(\boldsymbol{\varepsilon},d)+\psi_n^-(\boldsymbol{\varepsilon}) \tag{10}$$

in which,

$$\psi_n^+(\boldsymbol{\varepsilon},d)=\mathrm{g}(d)\frac{K}{2}\mathrm{Tr}^+(\boldsymbol{\varepsilon})^2 \tag{11a}$$

$$\psi_t(\boldsymbol{\varepsilon},d)=\mathrm{g}(d)\mu\boldsymbol{\varepsilon}_{\text{dev}}:\boldsymbol{\varepsilon}_{\text{dev}} \tag{11b}$$

$$\psi_n^-(\boldsymbol{\varepsilon})=\frac{K}{2}\mathrm{Tr}^-(\boldsymbol{\varepsilon})^2 \tag{11c}$$

Based on the volumetric and deviatoric splitting strategy of stored energy density, we reformulate a new Euler-Lagrange free energy functional $\Pi(\boldsymbol{\varepsilon},\Gamma)$ as

$$\begin{aligned}\Pi_{\ell_c}(\boldsymbol{\varepsilon},d)=&\underbrace{\int_{\Omega}g(d)\left[\frac{K}{2}\mathrm{Tr}^+(\boldsymbol{\varepsilon})^2+\mu\boldsymbol{\varepsilon}_{\text{dev}}:\boldsymbol{\varepsilon}_{\text{dev}}\right]d\Omega}_{\int_{\Omega}\left[\psi_n^+(\boldsymbol{\varepsilon},d)+\psi_t(\boldsymbol{\varepsilon},d)\right]d\Omega}+\\&\underbrace{\int_{\Omega}\frac{K}{2}\mathrm{Tr}^-(\boldsymbol{\varepsilon})^2 d\Omega}_{\int_{\Omega}\psi_n^-(\boldsymbol{\varepsilon})d\Omega}+\underbrace{\int_{\Omega}\mathcal{G}_c\gamma(d,\nabla d)\,d\Omega}_{\int_{\Omega}\psi_f(d)d\Omega}-\\&\underbrace{\int_{\Omega}\boldsymbol{b}^T\cdot\boldsymbol{u}\,d\Omega-\int_{\partial\Omega_t}\bar{\boldsymbol{t}}^T\cdot\boldsymbol{u}\,dS}_{W_{\text{ext}}(\boldsymbol{b},\boldsymbol{t},\boldsymbol{u})}\end{aligned} \tag{12}$$

Based on the variational principle, we can find the stationary form of this varitational problem for the admissible displacement field and the phase–field variable as follows,

$$\delta\Pi_{\ell_c}(\boldsymbol{\varepsilon},d)=\frac{\partial\Pi_{\ell_c}}{\partial\boldsymbol{u}}\cdot\delta\boldsymbol{u}+\frac{\partial\Pi_{\ell_c}}{\partial d}\cdot\delta d=0 \qquad (13)$$

Thus, we have

$$\delta\Pi_{\ell_c}(\boldsymbol{\varepsilon},d)=\underbrace{\int_\Omega\boldsymbol{\sigma}:\delta\boldsymbol{\varepsilon}d\Omega-\int_\Omega\boldsymbol{b}^T\cdot\boldsymbol{u}d\Omega-\int_{\partial\Omega_t}\bar{\boldsymbol{t}}^T\cdot\boldsymbol{u}dS}_{=\frac{\partial\Pi_{\ell_c}}{\partial\boldsymbol{u}}\cdot\delta\boldsymbol{u}}+\underbrace{\int_\Omega\mathcal{G}_c\left(\frac{1}{\ell_c}d\delta d+\ell_c\nabla d\cdot\delta\nabla d\right)d\Omega-\int_\Omega 2(1-d)\left(\psi_n^+(\boldsymbol{\varepsilon},d)+\psi_t(\boldsymbol{\varepsilon},d)\right)\delta d d\Omega}_{=\frac{\partial\Pi_{\ell_c}}{\partial d}\cdot\delta d} \qquad (14)$$

Now, we can obtain the balance of linear momentum as follows,

$$\nabla\cdot\boldsymbol{\sigma}(\boldsymbol{\varepsilon},d)+\boldsymbol{b}=0 \qquad (15a)$$

$$\boldsymbol{\sigma}(\boldsymbol{\varepsilon},d)\cdot\boldsymbol{n}=\bar{\boldsymbol{t}} \qquad (15b)$$

$$\boldsymbol{u}=\bar{\boldsymbol{u}} \qquad (15c)$$

In the new thermodynamically consistent phase–field model, the critical fracture energy release rate $\mathcal{G}_c$ in Griffith theory is decomposed into a mode-I fracture energy release rate $\mathcal{G}_{Ic}$ and a mode-II fracture energy release rate $\mathcal{G}_{IIc}$, as shown in Fig. 2a. On the basis of Benzeggagh-Kenane semi-empirical failure criterion (Benzeggagh and Kenane, 1996), the equivalent mixed mode I-II fracture energy release rate is expressed as

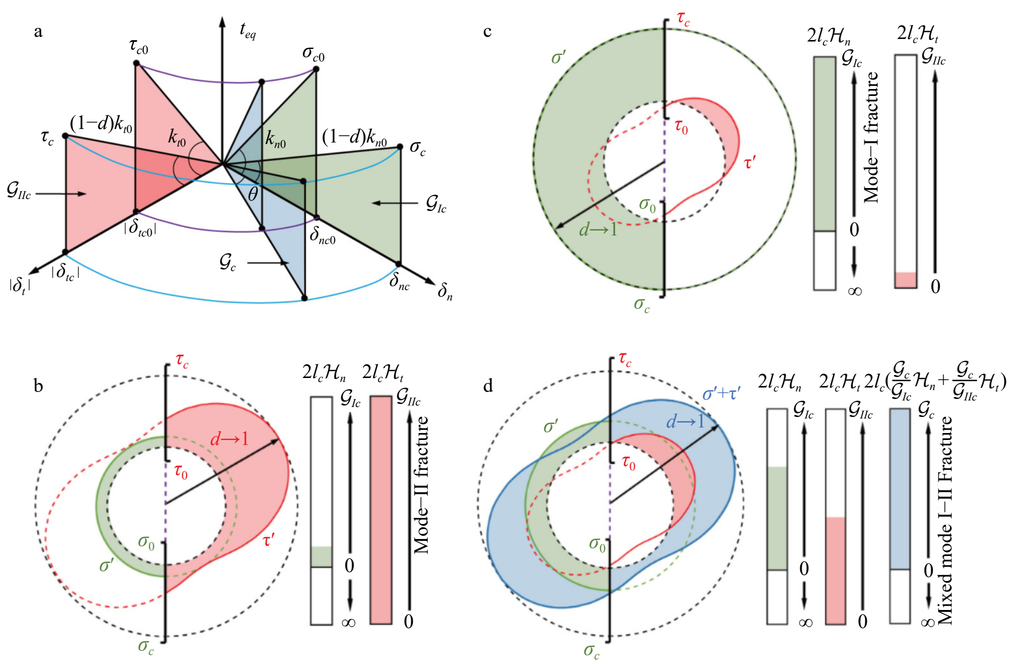

a—混合型断裂示意图；b—I型断裂驱动力示意图；c—II型断裂驱动力示意图；d—I–II混合型断裂驱动力示意图

图2 相场演化原理示意图

Fig. 2 Schematics of the phase-field evolution principles

(a) Mixed-mode fracture; (b) Mode-I fracture driving forces; (c) Mode-II fracture driving force; (d) Mixed mode I-II fracture driving forces

$$\begin{aligned}\mathcal{G}_c&=\mathcal{G}_{Ic}+(\mathcal{G}_{IIc}-\mathcal{G}_{Ic})\left(\frac{\mathcal{G}_{IIc}}{\mathcal{G}_{Ic}+\mathcal{G}_{IIc}}\right)^m\\&=\mathcal{G}_{Ic}+(\mathcal{G}_{IIc}-\mathcal{G}_{Ic})\left(\frac{\mathcal{H}_t}{\mathcal{H}}\right)^m\end{aligned} \qquad (16)$$

The normalized brittle fracture driving force can be formulated as,

$$\mathcal{F}=\frac{\mathcal{G}_I(\theta)}{\mathcal{G}_{Ic}}+\frac{\mathcal{G}_{II}(\theta)}{\mathcal{G}_{IIc}} \qquad (17)$$

and

$$\frac{\mathcal{H}}{\mathcal{G}_c}\simeq\eta\left(\frac{\mathcal{H}_n}{\mathcal{G}_{Ic}}+\frac{\mathcal{H}_t}{\mathcal{G}_{IIc}}\right) \qquad (18)$$

where $\frac{\mathcal{H}_n}{\mathcal{G}_{Ic}}$ is the normalized driving force for the purely tensile fractures caused by volumetric dilation, whereas $\frac{\mathcal{H}_t}{\mathcal{G}_{IIc}}$ is the normalized driving force for the fractures induced by deviatoric deformation. η is the corrected parameter to prevent instabilities, which is expressed as

$$\eta = \frac{\mathcal{H}(\mathcal{G}_{Ic}\mathcal{G}_{IIc})}{\mathcal{G}_c(\mathcal{H}_t\mathcal{G}_{Ic} + \mathcal{H}_n\mathcal{G}_{IIc})} \tag{19}$$

To prevent crack healing and ensure the energy conservation, the modified crack evolution equation with the new crack driving forces reaches the following form:

$$(1-d)\left(\frac{\mathcal{H}_n(\boldsymbol{\varepsilon},d)}{\mathcal{G}_{Ic}} + \frac{\mathcal{H}_t(\boldsymbol{\varepsilon},d)}{\mathcal{G}_{IIc}}\right)\eta + \frac{\ell_c}{2}\nabla^2 d - \frac{1}{2\ell_c}d = 0 \tag{20}$$

The normalized mixed-mode fracture driving forces read

$$\mathcal{H}_m = \frac{1}{\mathcal{G}_{Ic}}\mathcal{H}_n + \frac{1}{\mathcal{G}_{IIc}}\mathcal{H}_t \tag{21}$$

where

$$\begin{aligned}\mathcal{H}_n(\boldsymbol{\varepsilon},d) &= \max_{0\le t\le T}\left\{\psi_n^+(\boldsymbol{\varepsilon},d)\right\}\\ &= \max_{0\le t\le T}\left\{\frac{1}{2}\boldsymbol{\varepsilon}_{\text{sph}} : \mathbb{C} : \boldsymbol{\varepsilon}_{\text{sph}}, d_c\right\} \quad \mathrm{Tr}(\boldsymbol{\varepsilon}) \ge 0\end{aligned} \tag{22a}$$

$$\mathcal{H}_n(\boldsymbol{\varepsilon},d) = 0 \quad \mathrm{Tr}(\boldsymbol{\varepsilon}) < 0 \tag{22b}$$

$$\mathcal{H}_t(\boldsymbol{\varepsilon},d) = \max_{0\le t\le T}\{\psi_t(\boldsymbol{\varepsilon},d)\} = \max_{0\le t\le T}\left\{\frac{1}{2}\boldsymbol{\varepsilon}_{\text{dev}} : \mathbb{C} : \boldsymbol{\varepsilon}_{\text{dev}}, d_c\right\} \tag{22}$$

The schematic diagram of relationship between stored strain energy densities and occurrence of different types of fracture is depicted in Figs. 2b–2d.

The phase–field model is commonly solved within finite element (FE) framework (Liu et al., 2022). To begin FE approximation, the phase–field model aims to find an admissible displacement field u and an admissible phase–field d that satisfies the minimization of the total Euler–Lagrange free energy functional.

$$\{\boldsymbol{u}(\boldsymbol{x}), d(\boldsymbol{x})\} = \underset{\boldsymbol{u}\in\mathcal{S}_u, d\in\mathcal{S}_d}{\operatorname{argmin}} \Pi_{\ell_c}(\boldsymbol{\varepsilon}(\boldsymbol{u}), d) \tag{23}$$

where $\mathcal{S}_u$ and $\mathcal{S}_d$ are the admissible displacement field space and admissible phase–field space, respectively.

In the fully monolithic solution strategy, the trial displacement and phase–fields can be computed by the following linear system of equations.

$$\begin{bmatrix} \mathcal{K}^{uu} & \mathcal{K}^{ud} \\ \mathcal{K}^{du} & \mathcal{K}^{dd} \end{bmatrix} \begin{bmatrix} \delta u \\ \delta d \end{bmatrix} = \begin{bmatrix} \mathcal{R}^{u} \\ \mathcal{R}^{d} \end{bmatrix} \tag{24}$$

The external loads are applied in a stepwise manner. For the time interval $[t, t+1]$, the following linear system of equations reads

$$\begin{bmatrix} \boldsymbol{u}_I^{t+1} \\ d_I^{t+1} \end{bmatrix} = \begin{bmatrix} \mathcal{K}_t^{uu} & \mathcal{K}_t^{ud} \\ \mathcal{K}_t^{du} & \mathcal{K}_t^{dd} \end{bmatrix}^{-1} \cdot \begin{bmatrix} \mathcal{R}_I^{u,t+1} \\ \mathcal{R}_I^{d,t+1} \end{bmatrix} \tag{25}$$

2 Phase–field approach for strain localization

In the phase–field approach, the surface of discontinuity may include fractures (strong discontinuities) and deformation bands (weak discontinuities), as shown in Figs. 3a and 3b), and is represented by the expression

$$\Gamma_B = \int_{\Gamma} dS = \int_{\Omega} \gamma(d, \nabla d)\, d\Omega \tag{26}$$

where $\gamma(d,\nabla d)$ denotes the discontinuous surface density function, whose distribution is given in terms of an internal characteristic length ℓ_c as

$$\gamma(d,\nabla d) = \frac{1}{2\ell_c}d^2 + \frac{\ell_c}{2}|\nabla d|^2 \tag{27}$$

Let $\Psi(\boldsymbol{\varepsilon},\boldsymbol{\alpha})$ be the total free energy function in Ω, where the $\boldsymbol{\varepsilon}$ is the infinitesimal strain tensor and $\boldsymbol{\alpha}$ is the vector of strain-like plastic internal variables. In the presence of a deformation band, the regularized form of Ψ, denoted as Ψ_ℓ, may be developed by introducing the phase–field variable d and its gradient ∇d as follows (Braathen et al., 2020)

$$\begin{aligned}\Psi_{\ell_c}(\varepsilon,\alpha,d,\nabla d) &= \Psi_o(\varepsilon,\alpha,d) + \Psi_i(d,\nabla d)\\ &= \int_{\Omega}\psi_o(\varepsilon,\alpha,d)\,d\Omega + \int_{\Omega}\psi_i(d,\nabla d)\,d\Omega\end{aligned} \tag{28}$$

in which, Ψ_o and Ψ_i are the total free energies “outside” and “inside” the band, respectively.

Based on the assumption of elastic energy depending only on the elastic strains and the plastic energy depending only on the plastic strains (Collins and Houlsby, 1997), the free energy density ψ_o can be decomposed into the following form:

$$\psi_o(\boldsymbol{\varepsilon},\boldsymbol{\alpha},d) = \psi_o^e(\boldsymbol{\varepsilon}^e,d) + \psi_o^p(\boldsymbol{\varepsilon}^p,\boldsymbol{\alpha},d) \tag{29}$$

where ψ_o^e and ψ_o^p denote the elastic and plastic parts of ψ_o, respectively. For isothermal process, the second law of thermodynamics can then be stated in the form of the Clausius–Planck inequality and the dissipation function can be written as

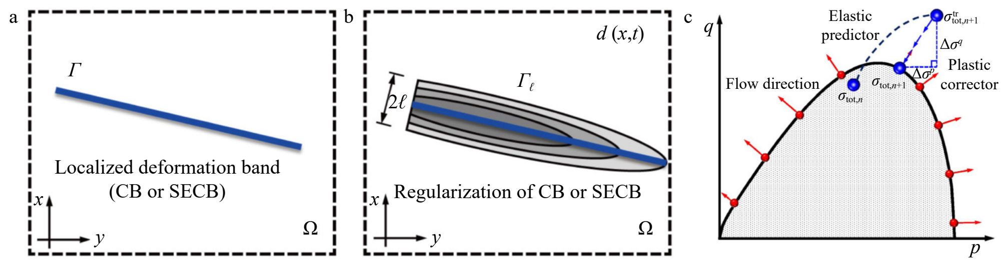

a—局部化带的尖锐拓扑结构；b—相场正则化变形带；c—不同围压下的流动方向示意图及其广义回归映射几何解释

图 3　应变损伤局部化的相场示意图

Fig. 3　Phase–field schematics of strain localization

(a) Sharp topology of localization zones; (b) The relevant phase–field regularized deformation bands; (c) Schematics of flow directions at different confining pressures and the general return mapping geometric interpretation

$$\sigma:\dot{\varepsilon}-\dot{\psi}_o^e\geq 0 \text{ and } \mathcal{D}^p=\dot{\psi}_o^p+\dot{\psi}_i\geq \qquad (30)$$

in which $\dot{\psi}_o^p$ represents the plastic dissipation in the bulk volume whereas $\dot{\psi}_i$ represents the plastic dissipation due to the formation and propagation of the deformation band.

Now, the Helmholtz free energy density in the computational domain can be decomposed into three parts as

$$\psi=\psi_o^e(\varepsilon^e,r,d)+\psi_o^p(\varepsilon^p,\alpha,d)+\psi_i(d,\nabla d) \qquad (31)$$

The elastic strain rate is further decomposed into volumetric and deviatoric parts:

$$\dot{\varepsilon}=\dot{\varepsilon}^e+\dot{\varepsilon}^p \qquad (32a)$$

$$\dot{\varepsilon}^e=\dot{\varepsilon}^e_{\text{vol}}+\dot{\varepsilon}^e_{\text{dev}} \qquad (32b)$$

$$\dot{\varepsilon}^p=\dot{\varepsilon}^p_{\text{vol}}+\dot{\varepsilon}^p_{\text{dev}} \qquad (32c)$$

where $\boldsymbol{\varepsilon}^e_{\text{vol}}$ and $\boldsymbol{\varepsilon}^e_{\text{dev}}$ are the volumetric and deviatoric parts, respectively.

Taking the purely volumetric dilatational part ψ^{e+}_{vol}, purely volumetric compressive part ψ^{e-}_{vol}, and mixed tensile-compressive-shear deformation part ψ^{e}_{dev} into consideration, the stored elastic energy density is then written as

$$\psi_o^e(\varepsilon^e,r,d)=\psi^{e+}_{\text{vol}}(\varepsilon^e,r,d)+\psi^{e}_{\text{dev}}(\varepsilon^e,r,d)+\psi^{e-}_{\text{vol}}(\varepsilon^e,r,d) \qquad (33)$$

where

$$\psi^{e+}_{\text{vol}}(\varepsilon^e,r,d)=g_1(d,r)\frac{K^e}{2}\text{Tr}^+(\boldsymbol{\varepsilon})^2 \qquad (34a)$$

$$\psi^{e}_{\text{dev}}(\varepsilon^e,r,d)=g_1(d,r)\mu^e\boldsymbol{\varepsilon}^e_{\text{dev}}:\boldsymbol{\varepsilon}^e_{\text{dev}} \qquad (34b)$$

$$\psi^{e-}_{\text{vol}}(\varepsilon^e,r,d)=g_1(d,r)\theta\frac{K^e}{2}\text{Tr}^-(\boldsymbol{\varepsilon})^2+(1-\theta)\frac{K^e}{2}\text{Tr}^-(\boldsymbol{\varepsilon})^2 \qquad (34c)$$

Next, we can write about the plastic energy density ψ_o^p as

$$\psi_o^p=\psi^p_{\text{vol}}+g_2(d)\psi^p_{\text{dev}} \qquad (35)$$

where $g_2(d)=(1-d)^2$ is another degradation function for describing the plastic-driven dissipation due to grain friction and grain arrangement during the deformation band processes. The mathematical expression of volumetric and deviatoric parts can be expressed as

$$\psi^p_{\text{vol}}=\int_0^t\boldsymbol{\sigma}:\dot{\boldsymbol{\varepsilon}}^p_{\text{vol}}d\tau \qquad (36a)$$

$$\psi^p_{\text{dev}}=\int_0^t\boldsymbol{\sigma}:\dot{\boldsymbol{\varepsilon}}^p_{\text{dev}}d\tau \qquad (36b)$$

Then, we derive the evolution of the phase–field variable d from the regularized total potential energy given by the expression

$$\Pi_{\ell_c}=\Psi_{\ell_c}+\Upsilon+\mathcal{K}-W \qquad (37)$$

where Ψ_{ℓ_c} is the total free energy, Υ is the work done by the viscous force $\mathcal{R}$ in forming and propagating the band, $\mathcal{K}$ is the kinetic energy. The total free energy can be written as

$$\Psi_{\ell_c}=\int_\Omega(\psi_o+\psi_i)d\Omega=\int_\Omega\left(\psi_o^e+\psi_o^p+\psi_i\right)d\Omega \qquad (38)$$

Taking the stationary point of Π_{ℓ_c} with respect to d and localizing gives the evolution equation becomes

$$\frac{\partial\Pi_{\ell_c}}{\partial d}=0\Rightarrow\mathcal{G}_c\ell_c\nabla^2 d-\mathcal{G}_c\frac{d}{\ell_c}-\frac{\partial\psi_o}{\partial d}=\frac{\mathcal{G}_c}{\ell_c}\zeta\dot{d} \qquad (39)$$

in which,

$$\frac{\partial\psi_o}{\partial d}=-2(1-d)^{2r-1}\left[r\left(\psi^{e+}_{\text{vol}}+\psi^{e}_{\text{dev}}+\theta\psi^{e-}_{\text{vol}}\right)\right]-2(1-d)\psi^p_{\text{dev}} \qquad (40)$$

Now, the strong form of the phase–field evolution for localized failure at any material point can then be written as

$$\zeta \dot{d} = \mathcal{H}^{\mathrm{eq}}(\boldsymbol{\varepsilon}, \boldsymbol{\varepsilon}^p, \boldsymbol{\alpha}, d) - \left(d - \ell_c^2 \nabla^2 d\right) \tag{41}$$

which is subjected to the following constraints.

$$d(\boldsymbol{x}, t) \in [0,1]; \dot{d}(\boldsymbol{x}, t) \geq 0; \mathcal{H}^{\mathrm{eq}}(\boldsymbol{\varepsilon}, \boldsymbol{\varepsilon}^p, \boldsymbol{\alpha}, d) \geq 0 \tag{42}$$

In the phase–field formulation for localized plastic deformation, we adopt a stress decomposition based on thermodynamic consistency.

$$\boldsymbol{\sigma} = \boldsymbol{\xi} + \boldsymbol{\chi} \tag{43}$$

where $\boldsymbol{\xi}$ is the shift and $\boldsymbol{\chi}$ denotes the dissipative stress tensors to Ziegler's orthogonality hypothesis（Ziegler, 2012）In our phase–field model for localized deformation bands in geological media, the shift and dissipative stress tensor can be stress tensor can be written as follows,

$$\boldsymbol{\xi} = g_2(d) \frac{\partial \psi_{\mathrm{dev}}^p(\boldsymbol{\varepsilon}^p, \boldsymbol{\alpha})}{\partial \boldsymbol{\varepsilon}^p} + \frac{\partial \psi_{\mathrm{vol}}^p(\boldsymbol{\varepsilon}^p, \boldsymbol{\alpha})}{\partial \boldsymbol{\varepsilon}^p} \tag{44a}$$

$$\boldsymbol{\chi} = g_2(d) \frac{\partial \psi_{\mathrm{dev}}^p(\boldsymbol{\varepsilon}^p, \boldsymbol{\alpha})}{\partial \boldsymbol{\alpha}} + \frac{\partial \psi_{\mathrm{vol}}^p(\boldsymbol{\varepsilon}^p, \boldsymbol{\alpha})}{\partial \boldsymbol{\alpha}} \tag{44b}$$

The corresponding shift pressure $\hat{\rho}$ and dissipative pressures π are defined as

$$\hat{\rho} = -\frac{1}{3}\mathrm{Tr}(\boldsymbol{\xi}) \pi = -\frac{1}{3}\mathrm{Tr}\left(\boldsymbol{\chi}\right) \tag{45}$$

which results in the effective pressure and the deviatoric stress invariant as follows

$$\mathcal{P} = \hat{\rho} + \pi \mathcal{Q} = \mathcal{J}_2\left(\boldsymbol{\chi}\right) \tag{46}$$

where $\mathcal{Q}$ is the von Mises dissipative stress and the effective pressure $\mathcal{P}$ in compression is regarded as positive.

Considering degradation due to brittle-like grain crushing, we can write the evolution of shift pressure for describing the porosity collapse as follows,

$$\hat{\rho} = \frac{1}{2}\gamma \mathcal{P}_c^0 \exp\left(\frac{\boldsymbol{\varepsilon}_{\mathrm{vol}}^p}{\Lambda_c} + \frac{1 - g_1(d)}{\Lambda_d}\right) \tag{47}$$

where Λ_c is the plastic compressibility and $\mathcal{P}_c^0$ denotes the initial preconsolidation pressure.

The local yield surface $\mathcal{F}(\pi, \mathcal{Q})$ in the dissipative stress space $(\pi, \mathcal{Q})$ is adopted as

$$\mathcal{F}(\pi, \mathcal{Q}) = \sqrt{\frac{\pi^2}{\mathcal{A}^2} + \frac{\mathcal{Q}^2}{\mathcal{B}^2}} - 1 \leq 0 \tag{48}$$

where $\mathcal{A}$ and $\mathcal{B}$ are coefficients defining the shape of the yield surface, which are given by the expressions.

$$\mathcal{A} = (1-\gamma)\mathcal{P} + \frac{1}{2}\gamma \mathcal{P}_c \tag{49a}$$

$$\mathcal{B} = \mu\left[(1-\alpha)\mathcal{P} + \frac{1}{2}\alpha\gamma \mathcal{P}_c\right] \tag{49b}$$

The driving force for the evolution of localized failure bands is defined as

$$\mathcal{H}^{\mathrm{eq}}(\boldsymbol{\varepsilon}, \boldsymbol{\varepsilon}^p, \boldsymbol{\alpha}, d) = \mathcal{H}^e(\boldsymbol{\varepsilon}^e, r, d) + \mathcal{H}^p(\boldsymbol{\varepsilon}^p, \boldsymbol{\alpha}, d) \tag{50}$$

where the elastic and plastic contributions are given by

$$\begin{aligned}\mathcal{H}^e(\boldsymbol{\varepsilon}, r, d) &= \mathcal{H}_{\mathrm{vol}}^{e+}(\boldsymbol{\varepsilon}^e, r, d) + \mathcal{H}_{\mathrm{dev}}^e(\boldsymbol{\varepsilon}^e, r, d) + \mathcal{H}_{\mathrm{vol}}^{e-}(\boldsymbol{\varepsilon}^e, r, d) \\ &= \max_{0 \leq t \leq T}\left\{\boldsymbol{\sigma}(\boldsymbol{\varepsilon}^e, d) : \left[\boldsymbol{\varepsilon}_{\mathrm{vol}}^{e+} + \theta \boldsymbol{\varepsilon}_{\mathrm{vol}}^{e-}\right] + \boldsymbol{\sigma}(\boldsymbol{\varepsilon}^e, d) : \boldsymbol{\varepsilon}_{\mathrm{dev}}^e\right\}\end{aligned} \tag{51a}$$

$$\begin{aligned}\mathcal{H}^p(\boldsymbol{\varepsilon}^p, \boldsymbol{\alpha}, d) &= \mathcal{H}_{\mathrm{vol}}^{p+}(\boldsymbol{\varepsilon}^p, \boldsymbol{\alpha}, d) + \mathcal{H}_{\mathrm{dev}}^p(\boldsymbol{\varepsilon}^p, \boldsymbol{\alpha}, d) \\ &= \int_0^t \left[\boldsymbol{\sigma}(\boldsymbol{\varepsilon}^e, d) : \left(\dot{\boldsymbol{\varepsilon}}_{\mathrm{vol}}^{p+} + \dot{\boldsymbol{\varepsilon}}_{\mathrm{dev}}^p\right)\right] d\tau\end{aligned} \tag{51b}$$

3 Numerical simulations of rock brittle fracture processes

To show the performance of our model, several fissured rock-like samples in the uniaxial compression tests are simulated. There are two kinds of fissured samples with dimensions of 76 mm ×152 mm, including one with a single preexisting fissure, and the other one containing three preexisting fissures, as shown in Fig. 4. The bottom boundary conditions are fixed, and a prescribed displacement field is applied on the top one. Following Xu and Li (2019), the rock-like material properties are chosen as follows: Young's modulus $E = 30.0$ MPa, Poisson's ratio $\upsilon = 0.3$, mode-I fracture energy release rate $\mathcal{G}_{Ic} = 5.0$ J/m2 and mode-II fracture energy release rate $\mathcal{G}_{IIc} = 13.0$ J/m2. The numerical samples are discretized into irregular triangular elements with the minimum size of $h_{\min} = 0.5$ mm and the maximum size of $h_{\max} = 0.5$ mm. The characteristic length in this phase–field modelling is adopted as $\ell_c = 1.0$ mm.

Numerical results of the single fissured rock-like sample subjected to the uniaxial compressive loads are plotted in Fig. 5, which describes the progressive failure process of rock-like sample containing one single preexisting fissure with an inclination angle of $\alpha = 45°$. The evolutions of crack growth paths and the maximum principal stress distribution are plotted in Figs. 5a and 5b, respectively. The tensile wing cracks driven by the maximum principal stress and the compressive-shear secondary cracks can be successfully reproduced. For validation, the current phase–field modelling results are compared with the previous experimental data (Xu and Li, 2019), as shown in Fig. 5c. The predicted fracture pattern

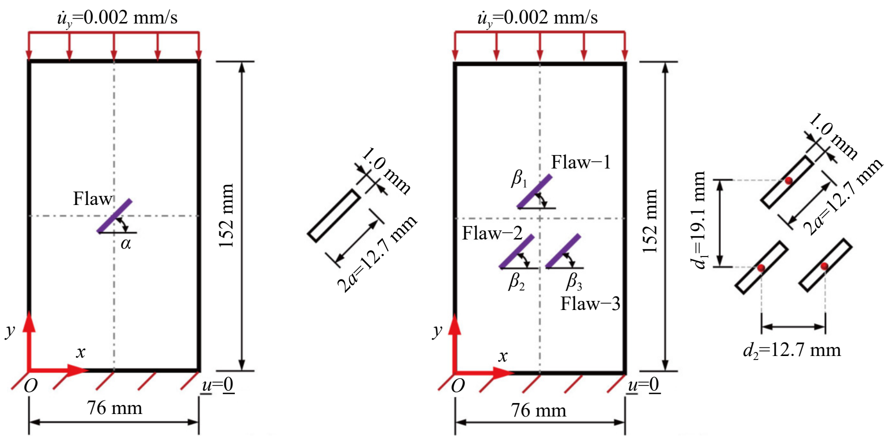

图 4　含单条预制裂隙和 3 条预制裂隙的类岩试样在单轴压缩试验中的几何形状及边界条件

Fig. 4　Geometry and boundary conditions of fissured rock-like specimens in the uniaxial compression tests: a single preexisting fissure and three preexisting fissures

agrees well with that observed in laboratory tests. The axial load—axial displacement curve obtained from simulations also show a reasonable agreement with that measured from laboratory experiments.

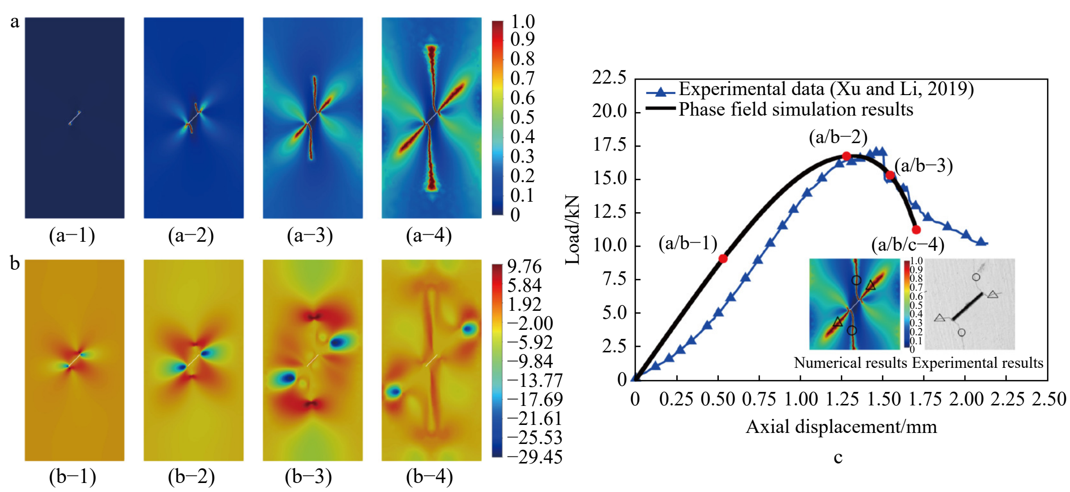

a—裂纹扩展路径；b—最大主应力分布；c—与实验结果的对比（Xu and Li, 2019）

图 5　含单条裂隙的类岩试样在单轴压缩试验中的渐进破坏过程

Fig. 5　Progressive failure process of a fissured rock-like sample consisting of a single fissure in the uniaxial compression test

(a) Crack growth paths; (b) Maximum principal stress; (c) Compression with laboratory experiments (Xu and Li, 2019)

Fig. 6a shows the progressive failure process of the rock-like sample-II containing three preexisting fissures with the identical incline angles of 45°. As observed in Figs. 6a-1 and 6a-2, wing cracks are initiated from tips of the preexisting fissures, and propagate along the axial direction. With the increase of axial loading, wing cracks coalesce with secondary cracks in the rock bridge regions, as shown in Figs. 6a-3 and 6a-4. The spatiotemporal distribution of σ_1 in Fig. 6b indicates that wing cracks are driven by tensile stress, while the initiation and propagation of secondary cracks are caused by the concentrations of shear stresses. The comparison between numerical and experimental results (Xu and Li, 2019) of crack coalescence patterns with corresponding axial load versus axial displacement curves in Fig. 6c implies the robust and reliability of our phase–field model.

4 Numerical simulations of strain localization in high-porosity rocks

The numerical model replicates the geometry of the triaxial compression test on Bentheim sandstone, including two symmetric V-shaped notches to induce strain localization, as illustrated in Fig. 7. The material

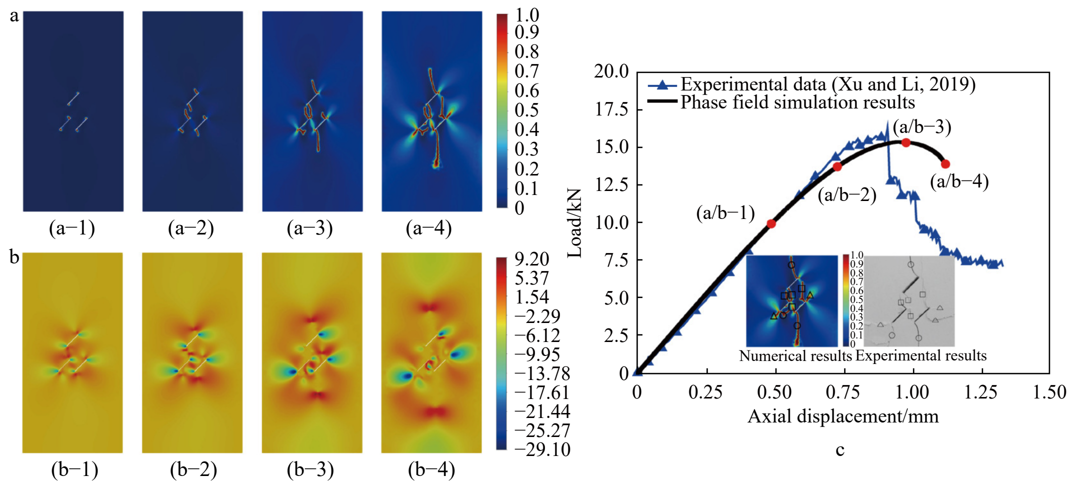

a—裂纹扩展路径；b—最大主应力分布；c—与实验结果的对比（Xu and Li, 2019）

图 6　含 3 条裂隙的类岩试样在单轴压缩试验中的渐进破坏过程

Fig. 6　Progressive failure process of a fissured rock-like sample containing three pre-existing fissures in the uniaxial compression test

(a) Crack growth paths; (b) Maximum principal stress; (c) Compression with laboratory experiments (Xu and Li, 2019)

parameters used in the simulation (Tembe et al., 2006, 2008; Ip and Borja, 2022) are summarized in Table 1. The following parameters for the plasticity model were assumed: $\mathcal{P}_c^0$=420 MPa, $\varepsilon^p_{eq.crit}=0.1$, $\mu=1.5$, $\alpha=0.5$ and $\gamma=1.0$. The computational time step was $\Delta t=1.0\times10^{-7}$ s and the length scale parameters was $\ell=0.6$ mm. A confining pressure of 250 MPa was applied, followed by axial loading at 2 μm/s to replicate the experimental setup.

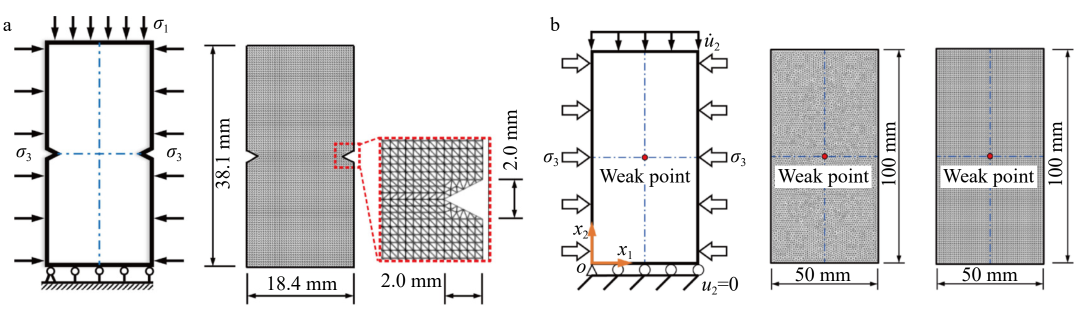

a—V 形缺口高孔隙砂岩试样；b—在三轴压缩试验中含有中心弱点的完整高孔隙砂岩试样的几何形状与边界条件

图 7　砂岩试样的几何形状与边界条件

Fig. 7　Geometric and boundary conditions of sandstone samples

(a) V-shaped notched high-porosity sandstone sample; (b) Intact high-porosity sandstone sample containing one centered weak point in triaxial compression tests

表 1　三轴压缩模拟的材料参数

Table 1　Material parameters for the triaxial compression simulation

Parameter	Symbol	Value	Unit
Mass density	ρ	2540	kg/m^3
Young’s modulus	E	19.2	GPa
Poisson’s ratio	ν	0.268	–
Critical fracture energy release rate	$\mathcal{G}_c$	1.0	J/m^2
Viscosity coefficient ratio	ζ	0.1	–
Plastic viscosity	η	5.0×10^{-3}	Pa^{-1}
Plastic compressibility	Λ_c	1.5×10^{-3}	–
Crushing potential	θ	0.1	–

The calculated vertical displacement u_2 and phase–field variable d are displayed in Figs. 8a and 8b, respectively. We observe that the compaction band first initiates at the tip of the two V-shape notches and propagates horizontally towards the center. The result is a thin compaction band oriented perpendicular to the major compressive stress, as shown in Figs. 8a and 8b. Six representative points corresponding to the snapshots shown in Figs. 8a and 8b are labeled in the stress–strain curve shown in Fig. 8c. Both simulations predicted an initially hardening response with comparable peak strengths. However, substantial softening is observed in the current simulation. Compared with the simulation of Ip and Borja (2022), the current simulation predicts a more pronounced re-hardening response after the compaction band has formed, like that observed in the laboratory experiments. Fig. 8d plots the initial yield stress predicted by the phase–field simulation on the deviatoric stress versus mean normal stress plane against the experimental data reported by Vajdova and Wong (2003) and the results of a theoretical analysis conducted by Tembe et al. (2006) employing linear elastic fracture mechanics (LEFM). The initial yield stress predicted by the phase–field simulation lies within the region defined by the experimental and theoretical curves. In addition, the insert in Fig. 8d also indicates that the failure initiation pattern during compaction band formation agrees well with both macroscopic and microscopic observations (Vajdova and Wong, 2003; Tembe et al., 2006).

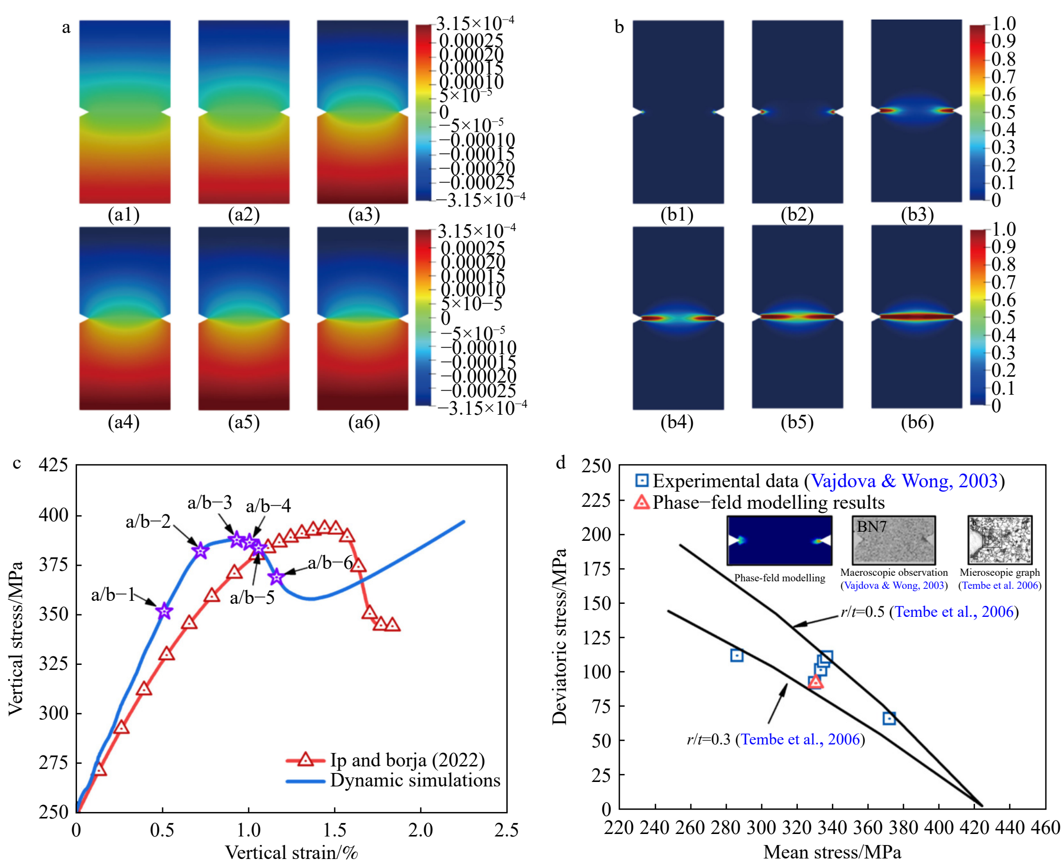

a—竖向位移场；b—压实带形成；c—模拟应力–应变曲线与 Ip and Borja（2022）的结果对比；d—相场模拟、实验（Vajdova and Wong, 2003）及 LEFM 理论分析（Tembe et al., 2006）得到的初始屈服应力

图 8 缺口砂岩试样中压实带形成的数值结果

Fig. 8 Numerical results of compaction bands formation

(a) Vertical displacement field (unit: m); (b) Compaction band formation; (c) Comparison of the simulated stress–strain response with the simulation result of Ip and Borja (2022); (d) Initial yield stress for the notched Bentheim sandstone samples obtained from the phase–field simulation, laboratory tests (Vajdova and Wong, 2003) and LEFM theoretical analysis (Tembe et al., 2006)

We also conducted a series of hypothetical numerical simulations on Bentheim sandstone samples to further demonstrate the capability and performance of the phase–field model. All simulations were conducted under 2D plane strain conditions on a rectangular sample having a width of 50 mm and a height of 100 mm, as seen in Fig. 7b. The boundary conditions and mechanical parameters can be found in Wang et al. (2023).

To investigate the effect of confining pressure on the dynamic strain localization and mechanical responses, we simulate six intact Bentheim sandstone samples in plane strain compression with different σ_3. The confining pressure σ_3 is changed from 10 MPa to 60 MPa in increments of 10 MPa. Fig. 10 shows the resulting localized deformation band patterns, suggesting that the confining pressure plays a critical role in the dynamic strain localization. When σ_3 increases from 10.0 MPa to 60.0 MPa, the localized deformation band pattern first changes from a dilation shear band with a high orientation angle (Figs. 9a and 9b) to a shear-enhanced compaction band with a medium inclination angle (Figs. 9c and 9d), towards a pure compaction band with a low inclination angle (Figs. 9e and 9f). The slightly curved shape of shear-enhanced compaction bands is caused by the combined compressive normal and shear stresses. These results indicate that our model can capture the transition from dilatant to compactive strain localization, which agrees with results from breakage mechanics theory.

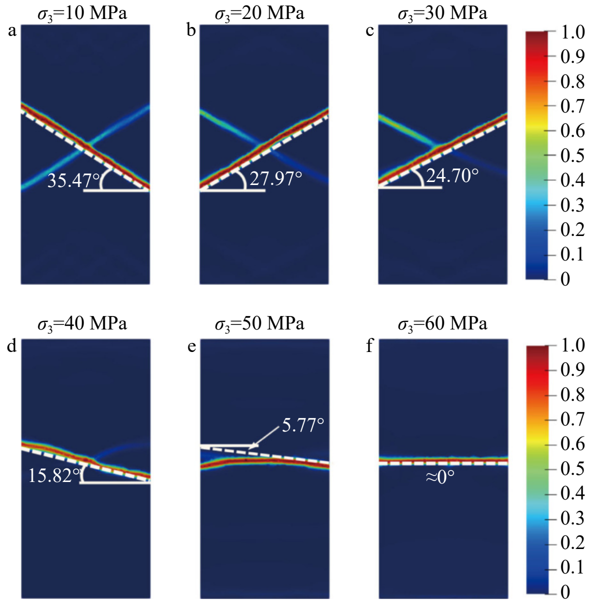

图 9　平面应变压缩试验中侧向应力 σ_3 对局部变形带形态的影响

Fig. 9　Effect of σ_3 on the localized deformation band patterns in the plane strain compression tests

Fig. 10a shows the relevant macro-mechanical axial stress versus axial strain curves for these six simulations. Fig. 10b performs the deviatoric stress $Q = \sigma_1 - \sigma_3$ versus axial strain at the different confining pressures. We observe that the confining pressure increases the localized deformation pattern transforms from a shear band type with significant strain softening, to shear-enhanced compaction band with moderate strain softening, to pure compaction band with pronounced strain hardening. This interesting phenomenon can be also illustrated by the graphic diagram of relationships between loading stress paths and the initial yield surface, as seen in Fig. 10c. The predicted $\varepsilon_{\mathrm{vol}} - \varepsilon_1$ curves are plotted in Fig. 10d. When the deformation band changes from a shear-band type to a pure compaction band, the minimum value of volumetric strain decreases. At the onset of localized deformation, we observe that the volumetric strain first decreases significantly due to grain crushing. At low confining pressures, the sample dilates at the post-failure stage due to grain friction and rearrangement. However, at high confining pressures the sample compacts, indicating that pore collapse and porosity reduction continue during the development of pure compaction bands.

5　Conclusions and future perspectives

In this work, we state a phase–field framework to simulate the evolution of discontinuous structures in geo-materials, including fracture and deformation bands. For the brittle fracture, our phase–field framework has the robust capability of capturing the different pure tensile, pure shear and mixed tensile/compressive–shear cracks, simultaneously. The crack coalescence patterns in rock materials can be successfully captured, which is helpful to better understand their underlying mechanisms. In new future, we will extend our phase–field framework to explore the behind mechanisms of anisotropic brittle fracture and supershear ruptures in geomechanics and geophysics. For the localized deformation bands, our phase–field model can separate degradation mechanisms of brittle-like fracture and plastic-like dissipation at the microscale. This numer-

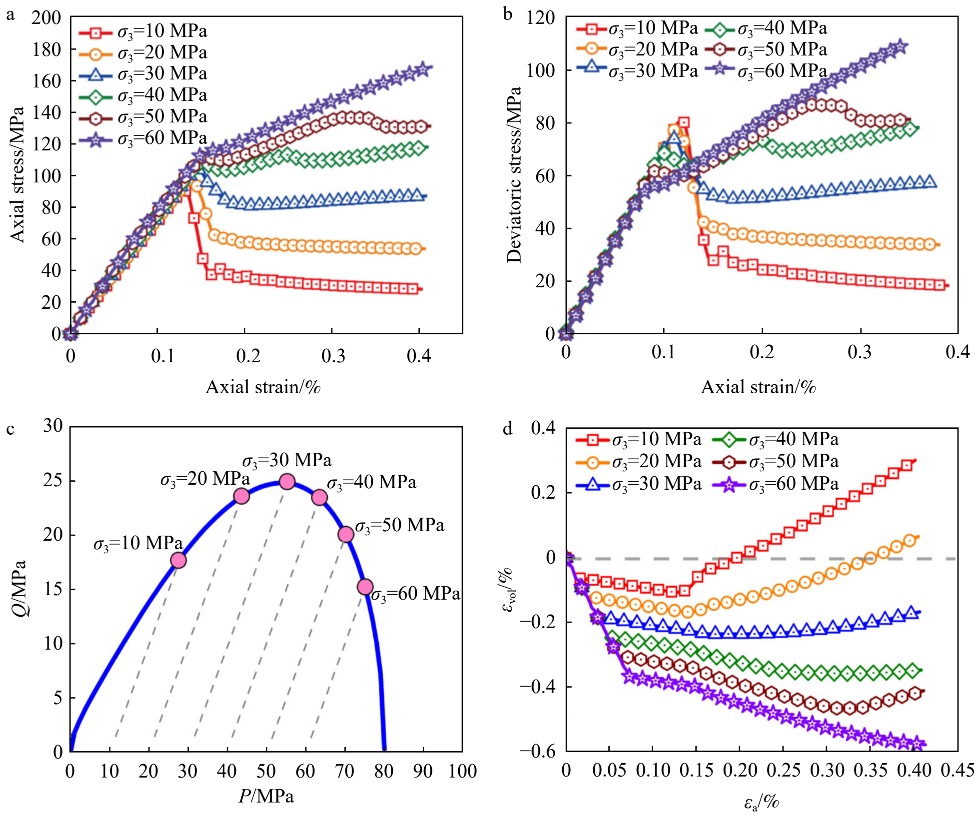

a—$\sigma_1-\varepsilon_1$ 曲线；b—$Q-\varepsilon_1$ 曲线；c—应力路径与初始屈服面关系；d—$\varepsilon_{vol}-\varepsilon_1$曲线

图 10 围压对力学响应的影响

Fig. 10 Effect of σ_3 on mechanical behavior

(a) σ_1–ε_1 curves; (b) Q–ε_1 curves; (c) Relations between loading stress paths and the initial yield surface; (d) $\varepsilon_{vol}-\varepsilon_1$ curves

ical model can successfully capture the transition between dilation shear bands and pure compaction bands. However, the current version of our phase–field model cannot consider complex multiphysics mechanisms, such as (i) chemically reactive transport and mineral alteration (dissolution–precipitation, cementation, damage healing); (ii) fully coupled non-isothermal two-phase flow with phase change (evaporation–condensation, freezing–thawing, hydrate dissociation) and capillary hysteresis; (iii) non-Darcy/Forchheimer flow and fluid inertia at high pore-Reynolds numbers; (iv) strong, history-dependent permeability anisotropy tied to fabric reorientation, dilation/compaction bands, and grain-scale rearrangement; (v) grain crushing and particle rotations (micropolar/Cosserat effects); (vi) rate-dependent viscoelastic–viscoplastic and thermal creep; and (vii) fully dynamic rupture with high-frequency wave effects, including supershear propagation. Incorporating these processes would require additional species/phase balance equations, rate-dependent constitutive laws with appropriate internal variables, micro-rotation kinematics, and explicit inertia with wave-speed constraints; these are outside the present scope and are left for future work.

附加材料：附图由作者提供，数据真实性由作者负责，在线查看网址：https://journal.geomech.ac.cn/cn/article/doi/10.12090/j.issn.1006-6616.2025149

References

ABDALLAH Y, SULEM J, BORNERT M, et al., 2021. Compaction banding in high - porosity carbonate rocks: 1. Experimental observations[J]. Journal of Geophysical Research: Solid Earth, 126(1): e2020JB020538.

AMOR H, MARIGO J J, MAURINI C, 2009. Regularized formulation of the variational brittle fracture with unilateral contact: numerical experiments[J]. Journal of the Mechanics and Physics of Solids, 57(8): 1209-1229.

BAUD P, KLEIN E, WONG T F, 2004. Compaction localization in porous sandstones: spatial evolution of damage and acoustic emission activity[J]. Journal of Structural Geology, 26(4): 603-624.

BAUD P, SCHUBNEL A, HEAP M, et al., 2017. Inelastic compaction in high - porosity limestone monitored using acoustic emissions[J]. Journal of Geophysical Research: Solid Earth, 122(12): 9989-10008.

BENZEGGAGH M L, KENANE M, 1996. Measurement of mixed-mode delamination fracture toughness of unidirectional glass/epoxy composites with mixed-mode bending apparatus[J]. Composites Science and Technology, 56(4): 439-449.

BERTRAND D, NICOT F, GOTTELAND P, et al., 2008. Discrete element method (DEM) numerical modeling of double-twisted hexagonal mesh[J]. Canadian Geotechnical Journal, 45(8): 1104-1117.

BOURDIN B, FRANCFORT G A, MARIGO J J, 2000. Numerical experiments in revisited brittle fracture[J]. Journal of the Mechanics and Physics of Solids, 48(4): 797-826.

BRAATHEN A, PETRIE E, NYSTUEN T, et al., 2020. Interaction of deformation bands and fractures during progressive strain in monocline-San Rafael Swell, Central Utah, USA[J]. Journal of Structural Geology, 141: 104219.

CAO Y J, WANG W, SHEN W Q, et al., 2022. A new hybrid phase-field model for modeling mixed-mode cracking process in anisotropic plastic rock-like materials[J]. International Journal of Plasticity, 157: 103395.

CHENG Y, WONG L N Y. (2018). Microscopic characterization of tensile and shear fracturing in progressive failure in marble[J]. Journal of Geophysical Research: Solid Earth, 123(1): 204-225.

COLLINS I F, HOULSBY G T, 1997. Application of thermomechanical principles to the modelling of geotechnical materials[J]. Proceedings of the Royal Society A: Mathematical, Physical and Engineering Sciences, 453(1964): 1975-2001.

CRUZ F, ROEHL D, DO AMARAL VARGAS JR E, 2018. An XFEM element to model intersections between hydraulic and natural fractures in porous rocks[J]. International Journal of Rock Mechanics and Mining Sciences, 112: 385-397.

DARVE F, SERVANT G, LAOUAFA F, et al., 2004. Failure in geomaterials: continuous and discrete analyses[J]. Computer Methods in Applied Mechanics and Engineering, 193(27-29): 3057-3085.

DESRUES J, CHAMBON R, 2002. Shear band analysis and shear moduli calibration[J]. International Journal of Solids and Structures, 39(13-14): 3757-3776.

FEI F, CHOO J, 2021. Double-phase-field formulation for mixed-mode fracture in rocks[J]. Computer Methods in Applied Mechanics and Engineering, 376: 113655.

FENG X T, XU H, QIU S L, et al., 2018. In situ observation of rock spalling in the deep tunnels of the China Jinping underground laboratory (2400 m depth)[J]. Rock Mechanics and Rock Engineering, 51(4): 1193-1213.

FOSSEN H, BALE A, 2007. Deformation bands and their influence on fluid flow[J]. AAPG Bulletin, 91(12): 1685-1700.

FOSSEN H, SCHULTZ R A, TORABI A, 2011. Conditions and implications for compaction band formation in the Navajo Sandstone, Utah[J]. Journal of Structural Geology, 33(10): 1477-1490.

FRANCFORT G A, MARIGO J J, 1998. Revisiting brittle fracture as an energy minimization problem[J]. Journal of the Mechanics and Physics of Solids, 46(8): 1319-1342.

GUDEHUS G, KARCHER C, 2024. Hydraulic breakthrough of clay smears due to technical and natural actions[J]. Acta Geotechnica, 19(6): 3283-3298.

HEIDER Y, 2021. A review on phase-field modeling of hydraulic fracturing[J]. Engineering Fracture Mechanics, 253: 107881.

HOEK E, 1968. Brittle fracture of rock[M]//STAGG K G, ZIENKIEWICZ O C. Rock mechanics in engineering practice. New York, John Wiley & Sons: 9-124.

HOLTZMAN B K, PATÉ A, PAISLEY J, et al., 2018. Machine learning reveals cyclic changes in seismic source spectra in geysers geothermal field[J]. Science Advances, 4(5): eaao2929.

HONG Y, ZHANG J F, ZHAO Y C, et al., 2024. Coupled hydro-mechanical XFEM analysis for multi-fracturing through an excavation driven by an underlying aquifer: a forensic case study[J]. Acta Geotechnica, 19(6): 3707-3727.

HUANG L C, BAUD P, CORDONNIER B, et al., 2019. Synchrotron X-ray imaging in 4D: multiscale failure and compaction localization in triaxially compressed porous limestone[J]. Earth and Planetary Science Letters, 528: 115831.

HUG L, POTTEN M, STOCKINGER G, et al., 2022. A three-field phase-field model for mixed-mode fracture in rock based on experimental determination of the mode II fracture toughness[J]. Engineering with Computers, 38(6): 5563-5581.

INGRAFFEA A R, HEUZE F E, 1980. Finite element models for rock fracture mechanics[J]. International Journal for Numerical and Analytical Methods in Geomechanics, 4(1): 25-43.

IP S C Y, BORJA R I, 2022. A phase - field approach for compaction band formation due to grain crushing[J]. International Journal for Numerical and Analytical Methods in Geomechanics, 46(16): 2965-2987.

IP S C Y, BORJA R I, 2023. Modeling heterogeneity and permeability evolution in a compaction band using a phase-field approach[J]. Journal of the Mechanics and Physics of Solids, 181: 105441.

KUHN C, SCHLÜTER A, MÜLLER R, 2015. On degradation functions in phase field fracture models[J]. Computational Materials Science, 108: 374-384.

LEE S, REBER J E, HAYMAN N W, et al., 2016. Investigation of wing crack formation with a combined phase - field and experimental approach[J]. Geophysical Research Letters, 43(15): 7946-7952.

LEUTHOLD J, GEROLYMATOU E, VERGARA M R, et al., 2021. Effect of compaction banding on the hydraulic properties of porous rock: part I—experimental investigation[J]. Rock Mechanics and Rock Engineering, 54(6): 2671-2683.

LIU S J, WANG Y T, PENG C, et al., 2022. A thermodynamically consistent phase field model for mixed-mode fracture in rock-like materials[J]. Computer Methods in Applied Mechanics and Engineering, 392: 114642.

LIU S J, WANG Y T, 2025. A thermodynamically consistent phase-field model for frictional fracture in rocks[J]. International Journal of Plasticity, 185: 104220.

MIEHE C, HOFACKER M, WELSCHINGER F, 2010. A phase field model for rate-independent crack propagation: robust algorithmic implementation based on operator splits[J]. Computer Methods in Applied Mechanics and Engineering, 199(45-48): 2765-2778.

MOËS N, DOLBOW J, BELYTSCHKO T, 1999. A finite element method for crack growth without remeshing[J]. International Journal for Numerical Methods in Engineering, 46(1): 131-150.

MOËS N, BELYTSCHKO T, 2002. Extended finite element method for cohesive crack growth[J]. Engineering Fracture Mechanics, 69(7): 813-833.

MOVAHED Z, 2022. Fracture classification on geological image logs[EB/OL]. https://alzare.com/online-course-detail-page/fracture-classification-on-geological-image-logs.

NINKHLAI A, 2011. Dreamstime[EB/OL]. https://www.dreamstime.com/stock-photo-contraction-desiccation-cracks-dry-earth-lack-water-soil-image93520801.

POTYONDY D O, CUNDALL P A, 2004. A bonded-particle model for rock[J]. International Journal of Rock Mechanics and Mining Sciences, 41(8): 1329-1364.

RECHBERGER C, FEY C, ZANGERL C, 2021. Structural characterisation, internal deformation, and kinematics of an active deep-seated rock slide in a valley glacier retreat area[J]. Engineering Geology, 286: 106048.

RUDNICKI J W, RICE J R, 1975. Conditions for the localization of deformation in pressure-sensitive dilatant materials[J]. Journal of the Mechanics and Physics of Solids, 23(6): 371-394.

SELVADURAI A P S, YU Q, 2005. Mechanics of a discontinuity in a geomaterial[J]. Computers and Geotechnics, 32(2): 92-106.

SILLING S A, 2000. Reformulation of elasticity theory for discontinuities and long-range forces[J]. Journal of the Mechanics and Physics of Solids, 48(1): 175-209.

SILLING S A, ASKARI E, 2005. A meshfree method based on the peridynamic model of solid mechanics[J]. Computers & Structures, 83(17-18): 1526-1535.

SILLING S A, EPTON M, WECKNER O, et al., 2007. Peridynamic states and constitutive modeling[J]. Journal of Elasticity, 88(2): 151-184.

TEMBE S, VAJDOVA V, WONG T F, et al., 2006. Initiation and propagation of strain localization in circumferentially notched samples of two porous sandstones[J]. Journal of Geophysical Research: Solid Earth, 111(B2): B02409.

TEMBE S, BAUD P, WONG T F, 2008. Stress conditions for the propagation of discrete compaction bands in porous sandstone[J]. Journal of Geophysical Research: Solid Earth, 113(B9): B09409.

VAJDOVA V, WONG T F, 2003. Incremental propagation of discrete compaction bands: acoustic emission and microstructural observations on circumferentially notched samples of Bentheim[J]. Geophysical Research Letters, 30(14): 1775.

VANNUCCHI P, 2025. From compaction to scaly fabric: the spectrum of deformation bands in geological media. Horizon Europe Marie Skłodowska-Curie Actions Staff Exchanges project LOC3G, 1st Doctoral School, Vienna, Austria.

VARDOULAKIS I, 1980. Shear band inclination and shear modulus of sand in biaxial tests[J]. International Journal for Numerical and Analytical Methods in Geomechanics, 4(2): 103-119.

WANG Q, FENG Y T, ZHOU W, et al., 2020. A phase-field model for mixed-mode fracture based on a unified tensile fracture criterion[J]. Computer Methods in Applied Mechanics and Engineering, 370: 113270.

WANG T, WAUTIER A, TANG C S, et al., 2024a. 3D DEM simulations of cyclic loading-induced densification and critical state convergence in granular soils[J]. Computers and Geotechnics, 173: 106559.

WANG Y T, ZHOU X P, XU X, 2016. Numerical simulation of propagation and coalescence of flaws in rock materials under compressive loads using the extended non-ordinary state-based peridynamics[J]. Engineering Fracture Mechanics, 163: 248-273.

WANG Y T, WU W, 2023. A bond-level energy-based peridynamics for mixed-mode fracture in rocks[J]. Computer Methods in Applied Mechanics and Engineering, 414: 116169.

WANG Y T, BORJA R I, WU W, 2023. Dynamic strain localization into a compaction band via a phase-field approach[J]. Journal of the Mechanics and Physics of Solids, 173: 105228.

WANG Y T, WANG S, SORANZO E, et al. , 2024b. Phase-field modeling of brittle failure in rockslides[M]//WU W, WANG Y T. Recent geotechnical research at BOKU. Cham: Springer: 241-264.

WAUTIER A, BONELLI S, NICOT F, 2019. DEM investigations of internal erosion: grain transport in the light of micromechanics[J]. International Journal for Numerical and Analytical Methods in Geomechanics, 43(1): 339-352.

WENG H H, AMPUERO J P, 2020. Continuum of earthquake rupture speeds enabled by oblique slip[J]. Nature Geoscience, 13(12): 817-821.

WU J Y, 2017. A unified phase-field theory for the mechanics of damage and quasi-brittle failure[J]. Journal of the Mechanics and Physics of Solids, 103: 72-99.

XU J, LI Z X, 2019. Crack propagation and coalescence of step-path failure in rocks[J]. Rock Mechanics and Rock Engineering, 52(4): 965-979.

ZHANG X, SLOAN S W, VIGNES C, et al., 2017. A modification of the phase-field model for mixed mode crack propagation in rock-like materials[J]. Computer Methods in Applied Mechanics and Engineering, 322: 123-136.

ZHANG J Z, ZHOU X P, 2022. Fracture process zone (FPZ) in quasi-brittle materials: Review and new insights from flawed granite subjected to uniaxial stress[J]. Engineering Fracture Mechanics, 274: 108795.

ZHOU X P, WANG Y T, 2021. State-of-the-art review on the progressive failure characteristics of geomaterials in peridynamic theory[J]. Journal of Engineering Mechanics, 147(1): 03120001.

ZIEGLER H, 2012. An introduction to thermomechanics (Vol. 21)[M]. 2nd ed. Amsterdam: Elsevier

第一作者简介:

王允腾，博士，奥地利维也纳自然资源与生命科学大学（BOKU University）特聘教授（Privatdozent）、博士生导师。2019 年获重庆大学博士学位，2019—2021 年于沙特阿卜杜拉国王科技大学（KAUST）从事博士后研究，2021 年入职奥地利维也纳自然资源与生命科学大学任高级研究员，并于 2024 年获得教授资格。长期致力于岩土力学、非局部连续介质力学、计算力学、断裂与应变局部化、数据驱动策略及岩土工程等研究领域。在 *Nature Communications*、*CMAME*、*JMPS*、*RMRE*、*IJP* 等国际知名 SCI 期刊上发表学术论文 50 余篇，总被引逾 3700 次，H 指数为 31。2023—2025 年连续入选“全球前 2% 顶尖科学家榜单”；主持包括 FWF Lise Meitner 项目、OeaD 科技合作项目、奥地利 FWF 面上项目及欧盟“地平线欧洲”玛丽·居里学者项目在内的科研课题 10 余项。曾获 *Acta Geotechnica* 最佳论文奖、中国岩石力学与工程学会最佳博士论文奖、中国岩石力学与工程学会自然科学特等奖、重庆市自然科学一等奖、2024 年度“欧洲华人十大科技领军人才”称号，2025 年度奥地利维也纳市“BOKU Best Paper Award”等多项荣誉。

通信作者简介:

吴伟教授（Univ.-Prof. Dr.-Ing. Wei WU），奥地利维也纳自然资源与生命科学大学（BOKU University）终身讲席教授、博士生导师、岩土工程研究所主任，维也纳“Otto Pregl 岩土工程研究基金”委员会主席。1982 年毕业于武汉大学，1985 年获西安理工大学岩土工程硕士学位，1993 年获德国卡尔斯鲁厄大学博士学位。1993—2003 年，先后在德国与瑞士多家国际岩土工程咨询公司任职，2003 年起受聘于 BOKU University，任终身教授。吴教授是奥地利仅有的四位岩土工程教授之一，曾入选“欧洲华人十大科技领军人才”。作为土体亚塑性本构模型理论的重要奠基人与推动者，他在本构理论、数值方法、室内与原位试验、离心机模型试验、边坡与隧道工程、垃圾填埋与地质灾害防控等方面开展了系统研究，在 SCI 期刊与国际会议发表论文 200 余篇；主持奥地利 FWF、欧盟第六框架计划、第七框架计划、“地平线 2020”计划及“地平线欧洲”计划等多项大型合作项目，并于近年荣获欧盟 ERC 高级研究基金（Advanced Grant）的殊荣。吴伟教授在学术传播与国际交流方面亦贡献卓著。他创办并担任岩土工程领域国际权威期刊 *Acta Geotechnica* 主编，同时兼任 Springer 出版社“岩土力学与工程”系列丛书主编，以及 *Canadian Geotechnical Journal* 等多个知名国际期刊的副主编。